Rapid detection and profiling of cancer cells in fine-needle aspirates

Hakho Lee[a,1], Tae-Jong Yoon[a,1], Jose-Luiz Figueiredo[a], Filip K. Swirski[a], and Ralph Weissleder[a,b,2]

[a]Center for Systems Biology, Massachusetts General Hospital, 185 Cambridge Street, CPZN 5206, Boston, MA 02114; and [b]Department of Systems Biology, Harvard Medical School, 200 Longwood Avenue, Alpert 536, Boston, MA 02115

There is a growing need for fast, highly sensitive and quantitative technologies to detect and profile unaltered cells in biological samples. Technologies in current clinical use are often time consuming, expensive, or require considerable sample sizes. Here, we report a diagnostic magnetic resonance (DMR) sensor that combines a miniaturized NMR probe with targeted magnetic nanoparticles for detection and molecular profiling of cancer cells. The sensor measures the transverse relaxation rate of water molecules in biological samples in which target cells of interest are labeled with magnetic nanoparticles. We achieved remarkable sensitivity improvements over our prior DMR prototypes by synthesizing new nanoparticles with higher transverse relaxivity and by optimizing assay protocols. We detected as few as 2 cancer cells in 1-μL sample volumes of unprocessed fine-needle aspirates of tumors and profiled the expression of several cellular markers in <15 min.

microfluidics | nanoparticle | nuclear magnetic resonance

Sensitive and quantitative technologies for molecular characterization of scant cells in easily accessible bodily sources (e.g., fine-needle aspirates (FNA), biopsies, whole blood, and other biological fluids) will have significant impact in life sciences and clinical practice (1, 2). If made available, such diagnostic platforms could be used for early detection/screening of cancer, comprehensive tumor characterization in patients, and targeted therapy based on personal responses to treatments (3, 4). The ideal detection technology would combine minimal sample processing with fast measurements, thus avoiding likely phenotypic/apoptotic changes of sampled cells. It would also allow for multiple biomarker detection in a single parent sample (multichannel detection) for accurate diagnosis (5). A number of sensors fulfilling some of these criteria have been developed based on optical (6, 7), electronic (8, 9), or magnetic detection (10, 11). The clinical utility of these systems, however, is limited, because they require lengthy sample purification or long assay times.

We recently developed a NMR-based sensor that offers fast detection of biological targets in native samples (12). Termed "DMR" for diagnostic magnetic resonance, the sensor measures the transverse relaxation rate (R_2) of water molecules in biological samples in which target molecules or cells of interest are labeled with magnetic nanoparticles (MNP).

Local magnetic fields created by the MNP accelerate the spin–spin relaxation of water protons, increasing the R_2 of samples (13) and thus providing a sensing mechanism. Because most biological objects have negligible magnetic susceptibilities, DMR measurements can be performed in unprocessed samples, allowing for fast assays. As proof-of-concept, we developed a prototype sensor (DMR-1) that detected bacteria, analytes, and abundant cancer cells (10^6 cells per mL) (12). Despite the underlying technological advantages, however, it has been difficult to achieve detection sensitivities ($\approx 10^3$ cells per mL) adequate for clinical applications.

The goal of the current study was to develop a DMR sensor with detection sensitivities and cellular profiling capabilities comparable with other standard methods (flow cytometry and Western blot analysis). This was achieved by developing (*i*) new magnetic nanoparticles with high transverse relaxivity, (*ii*) a NMR probe with

improved signal-to-noise ratio (SNR), and (*iii*) an analytical DMR protocol that can quantify the expression level of molecular markers in tumor cells. The clinical utility of the system (DMR-2) was evaluated by using FNA (14, 15) from a panel of xenograft tumor models. We detected as few as 2 cells in 1-μL volumes and analyzed cells for growth factor expression in nonpurified samples. DMR-2 exhibited detection sensitivities as good as those achieved with clinical methods (e.g., flow cytometry and Western blot analysis), but the assay was performed in much shorter time (in <15 min) and with smaller sample size.

Results

Optimized Magnetic Nanoparticles (MNP) for DMR Assay. The overall DMR sensitivity for cell detection is determined by 2 different sensitivities. The first is the cell-concentration sensitivity that depends on the r_2 relaxivities of MNP. For a given cell concentration, MNP with high r_2 relaxivities will induce large R_2 changes. The second sensitivity is related to the signal-to-noise ratio (SNR) of the NMR system. With a high SNR, the sample volume for NMR detection can be reduced, thus lowering the cell detection threshold (equal to cell concentration × sample volume).

To improve the DMR sensitivity, we first set out to increase the r_2 relaxivity of MNP. Because r_2 is proportional to $M^2 \cdot d^2$, where M and d are the magnetization and the diameter of MNP, respectively (16), high r_2 can be achieved by using materials with strong magnetization and by increasing the size of the magnetic core. On the other hand, MNP should still be small enough (<50 nm in hydrodynamic diameter) for optimal binding to cell surface and permeation into cells for intracellular marker targeting (17). Small MNP are also advantageous because they typically exhibit higher stability in isoosmolar solution (no sedimentation) and superparamagnetic behavior to avoid spontaneous magnetic aggregation (18, 19). In addition, the MNP should be hydrophilic and biocompatible so as not to alter the expression profiles of incubated cells (20).

Review of reported and commercially available MNP indicated that most materials (blue circle in Fig. 1*A*) were not ideally suited for DMR assays because of their large size and/or low relaxivity. We therefore developed and optimized MNP for DMR assays. We opted to base on ferrite MNP (21–25) and doped the particles with Mn^{2+} (Mn-MNP) to increase overall magnetization (M). We also adopted a seed-growth approach to increase the metallic core size (d). Fig. 1*B* shows an example of the Mn-MNP with a core size of 16 nm. To obtain these particles, we first synthesized 10-nm core seeds by reacting $Fe(acac)_3$, $Mn(acac)_2$ and 1,2-hexadecanediol at high temperature (300 °C). By repeating the seed-mediated growth, the magnetic cores were then incrementally grown to 12, 16, and 22

www.manaraa.com
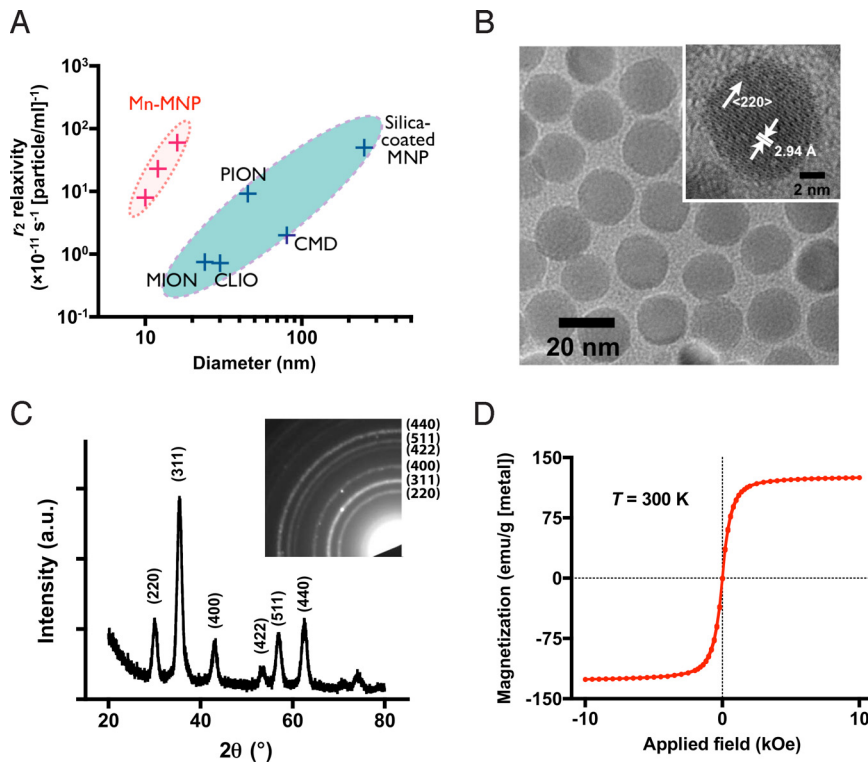
ENGINEERING

MEDICAL SCIENCES

Fig. 1. Class of magnetic nanoparticles for DMR assay. (*A*) To enhance the DMR sensitivity, we synthesized Mn-doped ferrite particles (Mn-MNP) with high r_2 relaxivities but still with small sizes ($d = 10, 12, 16$ nm; red circle). Compared with reported and commercially available MNP (blue circle), Mn-MNP assumed superior relaxivities with r_2 as high as 420 s^{-1}·mM^{-1}[metal] (equal to 6.0×10^{-11} s^{-1}·[particle per milliliter]$^{-1}$). Furthermore, Mn-MNP were highly stable in isoosmolar solution without sedimentation and magnetic aggregation. *d*, mean diameter of Mn-MNP. (*B*) Transmission electron microscope (TEM) images showed that all Mn-MNP ($d \leq 16$ nm) had a narrow size distribution (Fig. S1 *A* and *B*) and were highly crystalline (*Insets*). (*C*) Both the X-ray powder diffraction (XRD) and the electron diffraction patterns (*Inset*) revealed a typical spinel structure of ferrite. The crystal sizes, measured by fitting the major peaks (311) in XRD, were in agreement with the TEM estimation (Fig. S1*C*), confirming the single domain nature of Mn-MNP. (*D*) All Mn-MNP were superparamagnetic at 300 K. The magnetization increased with particle size, possibly because of reduced surface effects (e.g., spin-canting) in larger particles (Fig. S2 *A*). Thus, the r_2 relaxivity is the highest with the largest Mn-MNP ($d = 16$ nm; Fig. S2*B*). CLIO, cross-linked iron oxide; MION, monocrystalline iron oxide; PION, poly crystalline iron oxide; CMD, carboxymethyl dextran-coated MNP.

nm. The maximum diameter of Mn-MNP that did not exhibit aggregation in biocompatible media was $\approx$16 nm. Subsequently, Mn-MNP were rendered water soluble by coating the particle surface with small-molecule (2,3-dimercaptosuccinic acid; see *Methods* for details). Mn-MNP with diameter $\leq$16 nm were highly monodisperse [see supporting information (SI) Fig. S1], showed crystalline ferrite structure (Fig. 1*C*), and were superparamagnetic at 300 K (Fig. 1*D*). The magnetization was proportional to the particle diameter (Fig. S2*A*), which may be attributed to reduced spin-canting in larger particles (26). Compared with other ferrite MNP commercially available or previously reported, the Mn-MNP showed higher relaxivities for their sizes (red circle in Fig. 1*A*) with r_2 reaching $\approx$420 s^{-1}·mM^{-1}[Fe+Mn] (corresponding to 6.0×10^{-11} s^{-1}·[particle per milliliter]$^{-1}$) at 0.5 T (Fig. S2*B*). We rendered the 16-nm Mn-MNP specific for cancer cells by conjugating monoclonal antibodies (against HER2/*neu*, EGFR, or EpCAM; see *Methods* for details) to the particle surface. Approximately 10 antibody molecules were immobilized per particle, resulting in an overall hydrodynamic diameter of $\approx$20 nm. The targeted Mn-MNP exhibited long-term ($>$1 month) stability in physiological buffer solutions (pH $=$ 7.2).

NMR Probe with Higher SNR. Another important factor in determining the overall detection sensitivity is the SNR of a NMR setup. In the DMR-2 system, we improved the SNR by devising a NMR probe with high filling factor ($\approx$1) and low electrical noise. The probe consisted of a solenoidal microcoil embedded in a microfluidic structure (Fig. 2*A*). The coils were first wound around polyethylene tubes and subsequently immersed in a polymer (polydim-

ethylsiloxane). After polymer curing, the tubes were retracted to open up fluidic channels (see *Methods* for details). The entire bore of the solenoid thus can be filled with sample, resulting in $>$350% enhancement in NMR signal level (Fig. 2*B*). Compared with the lithographically patterned and metal-plated planar coils of the DMR-1 system (12), these solenoidal coils produced more homogeneous radio-frequency magnetic fields (27) and had less electrical resistance. With these advantages, the sample volume for the DMR-2 was reduced by a factor of 10 (to 1 μL) compared with DMR-1. At the same measurement conditions (NMR electronics and MNP), DMR-2 achieved 10-fold enhanced mass-detection sensitivity over the DMR-1.

Scaling Cellular Measurements. In current clinical practice, FNA diagnoses are primarily reported as the presence or absence of malignant cells in a specimen. The capability to quantify and profile cancer cells, however, would likely improve diagnosis. For example, a critical issue when screening cancer cells is how to correlate the expression levels of tumor markers to the number of malignant cells in a given sample. Without this knowledge, one could either measure high expression in relatively few cells or low expression in many cells.

To measure cell number by DMR, we exploited a previously characterized phenomenon of low-grade phagocytosis of nontargeted MNP by tumor cells (28, 29). When mammalian cells were incubated with unmodified MNP (MNP-$\varnothing$) for 5 min, linear and cell number-dependent R_2 changes ($\Delta R_2^{\varnothing}$) are observed (Fig. 3*A*). Interestingly, these changes were similar across a wide variety of cell types. The results were fitted to $\Delta R_2^{\varnothing} = r_2^{\varnothing} \cdot N$, where $r_2^{\varnothing}$ is the
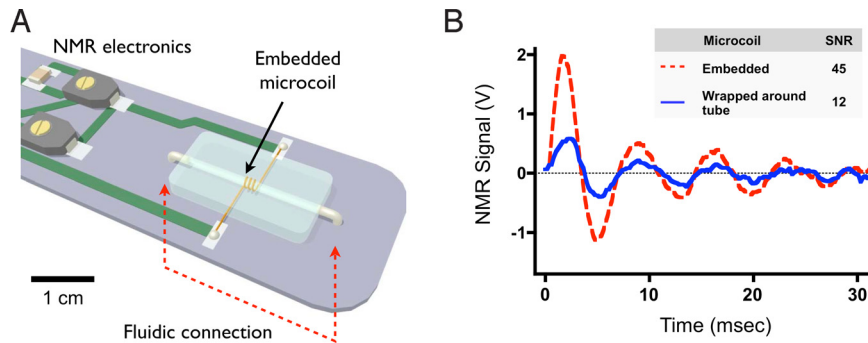
Lee et al.

www.manaraa.com

Fig. 2. DMR probe for higher sensitivity. (*A*) The probe consisted of a solenoidal coil embedded in a microfluidic device. Compared with the planar microcoils in the previous system, the solenoidal coil offered better NMR signal quality with less electrical noise. Furthermore, by embedding the solenoidal coil inside the microfluidic body, we could make the entire bore of the solenoidal coil available for samples, maximizing the filling factor ($\approx$1). The probe was mounted on a printed circuit board with NMR electronics and fluidic connector and packaged with other parts of a DMR system. (*B*) The DMR probe offered high SNR with its high filling factor. The enhancement, measured in the free induction decay of NMR signal (without averaging), was >350%.

relaxivity per cell (cellular relaxivity) for MNP-Ø and N is the number of cells in the DMR detection volume. The cellular relaxivities ($r_2^{\varnothing}$) were statistically identical ($P > 0.99$) among different tumor cell lines, making them a universal measure for estimating cell number. By applying this method to xenograft FNA samples (HCT116; Fig. 3*B*), we could estimate cell numbers in experimental samples. We further defined the expression level of a targeted marker as $\Delta R_2^{Ab}/\Delta R_2^{\varnothing} = (r_2^{Ab} \cdot N)/(r_2^{\varnothing} \cdot N) = r_2^{Ab}/r_2^{\varnothing}$, where ΔR_2^{Ab} and r_2^{Ab} are R_2 changes and the cellular relaxivity, respectively, with a marker-specific MNP. The DMR-2 assay, therefore, can report the cellular expression level of a specific marker.

Optimized Assay Protocol with High Specificity. Samples obtained from FNA, biopsies or blood are inherently complex in composition and variable in cell number. For a given detection method to be clinically useful, it has to be highly specific and robust under different sample conditions. To improve the specificity of the DMR assay, we first determined the level of interference from noncancerous host cells. Using HER2/*neu*-specific Mn-MNP (Mn-MNP-HER2) as a model system, we monitored the time-dependent cellular binding/uptake of particles in cancer cells and host cells, specifically leukocytes (Fig. 4*A*). As expected, T_2 (equal to $1/R_2$) changes increased in both cell types with longer incubation time, reflecting the well-known uptake kinetics in phagocytic cells (30). However, at shorter incubation times, the relative specificity of MNP to cancer cells was still high with negligible MNP binding to host cells. These observations led to an assay protocol that maximized cancer cell detection while minimizing the effect of host cells.

Compared with the previous method (30-min incubation) (12), this protocol was 6 times faster and improved the specificity >10-fold.

We further quantified the differences in cellular binding of cancer-targeted MNP between malignant and host cells. Mn-MNP-HER2 binding to cancer cells was much more avid, as verified by both fluorescent microscopy (Fig. 4*B*) and flow cytometry (Fig. 4*C*). The mean fluorescent intensity of MNP-targeted cancer cells was $>10^2$ times higher than those from leukocytes. DMR measurements resulted in similar differences with host cells having cellular relaxivities $\approx 10^{-6}$ s^{-1}·[cell per microliter]$^{-1}$, whereas cancer cells had cellular relaxivities $\approx 10^{-3}$ s^{-1}·[cell per microliter]$^{-1}$. The magnetic moment per cell, estimated from the relaxivities, were 10^{-7} and 10^{-10} emu for cancer and host cells, respectively. The magnetic fields from these cells can be measured by various magnetometers including Hall probes (31, 32), magnetoresistive elements (10, 11), and superconducting quantum interference devices (33). It is thus conceivable to combine DMR with a magnetic reader that can detect and sort cells according to cellular magnetic moments.

We also explored fast leukocyte depletion protocols to further enhance cancer cell detection, particularly in the whole blood where leukocytes are highly abundant. First, we investigated which leukocyte fraction would associate cancer-targeted MNP. Flow cytometry analysis revealed that nonspecific MNP binding/uptake was mostly by monocytes, neutrophils, NK cell and B cells (Fig. 4*C*). In repeat experiments, we removed these cells on the basis of CD11b (monocytes, neutrophils, NK cells) and B220 (B cells) expression. For the remaining host cells (mostly T cells), the MNP binding was
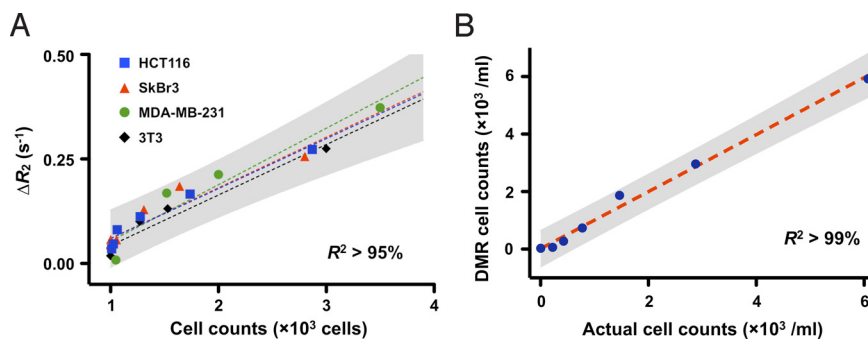

Fig. 3. Determination of cell counts in FNA. (*A*) The uptake of unmodified Mn-MNP (Mn-MNP-Ø) by cancer cells was exploited to estimate the cell population in aspirates. The measured R_2 changes were linearly proportional to the cell concentrations. Importantly, the linear trends were statistically identical in different cell types ($P > 0.99$). (*B*) The number of cells in actual FNA samples was estimated by DMR. After incubating samples with Mn-MNP-Ø, ΔR_2 was measured and converted to cell concentrations. The DMR estimation showed a good correlation with actual cell numbers counted with a hemocytometer. The gray areas in *A* and *B* indicate 95% prediction level from the linear fit.

Lee et al.

ENGINEERING
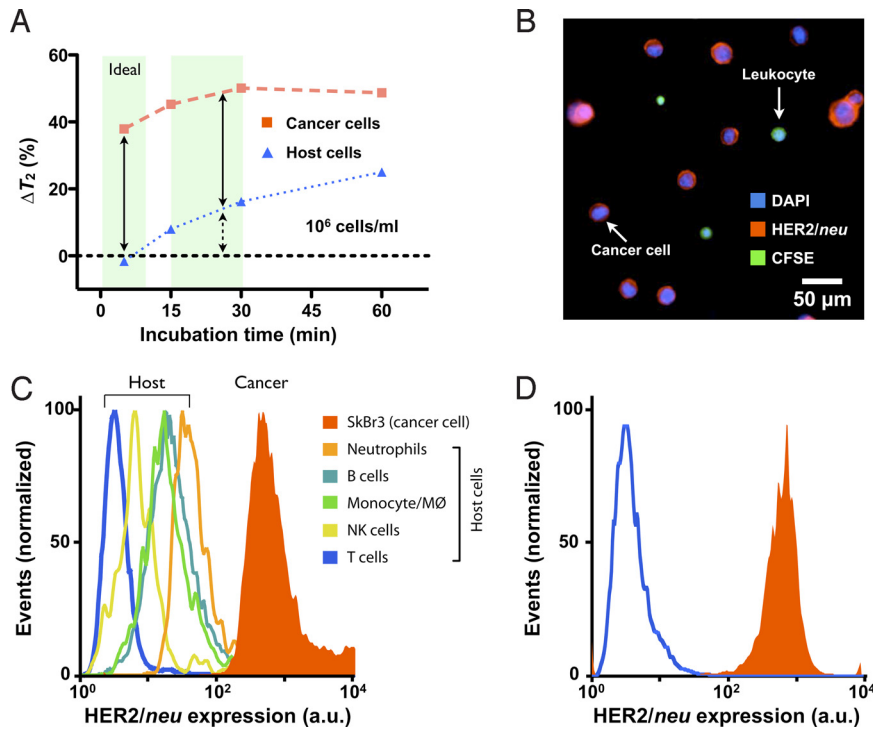
MEDICAL SCIENCES

www.manaraa.com

Fig. 4. Optimized assay protocol for maximal detection specificity. (*A*) The binding/uptake of cancer-targeted Mn-MNP by cancer cells and host cells was monitored with different incubation times. For cancer cells (SkBr3), ΔT_2 reached a plateau after 30 min of incubation, whereas ΔT_2 increased steadily for leukocytes over time. We thus adopted a short incubation time (5 min) to maximize the specificity. (*B* and *C*) Cancer cells (SkBr3) and leukocytes (prelabeled with CFSE) were incubated with fluorescent Mn-MNP-HER2. The micrograph (*B*) shows highly selective targeting of cancer cells by the particles. When the same samples were analyzed with flow cytometry, the cancer cells showed >10^2 times higher mean fluorescent intensity (MFI) than the host cells. Interestingly, the nonspecific uptake of MNP was mostly because of neutrophils, B cells, monocytes, and NK cells. (*D*) The host cell fraction responsible for high MNP uptake were further removed based on their surface markers (CD11b, B220). In the resulting sample, the specificity, measured by MFI, increased to >10^3. DAPI, 4′,6-diamidino-2-phenylindole; CFSE, carboxyfluorescein succinimidyl ester.

negligible (Fig. 4*D*). Combining shorter incubation times and negative cell selection, the specificity of cancer-targeted MNP over host cells in unpurified native samples is thus >10^3, which could be highly advantageous when profiling rare cells (<10 cells in 1 mL of blood) such as circulating tumor cells (4).

Tumor Cell Detection in FNA. To evaluate the above optimized DMR-2 assay, we obtained FNA from xenograft tumors in mice. Aliquots of freshly obtained aspirates were incubated with antibody-modified MNP for 5 min, washed to remove excess particles, and measured by the DMR-2 system in 1-μL samples (See *Methods* for details).

We first determined the detection sensitivity of DMR-2 by targeting the HER2/*neu* receptor on samples from BT474 xenografted breast cancers as a model system. The number of MNP per cell, quantified by ICP-AES (inductively coupled plasma atomic emission spectroscopy) was ≈5×10^5 (see *Methods*). When the same magnetically labeled cells were measured with the DMR sensor, a linear R_2 change ($R^2 > 99\%$) was observed at different cell concentrations (Fig. 5*A*). The relaxivity per cell (cellular relaxivity), obtained by fitting the titration curve, was ≈2.3×10^{-3} s^{-1}·[cell per microliter]$^{-1}$; the number of MNP in a cell, estimated from the cellular relaxivity was ≈10^5, which is in good agreement with the ICP-AES measurement. The detection limit was nearly at the single cell level (≈2 cells in 1-μL detection volume), far surpassing the sensitivities of our previous results (≈10^3 cells in 10-μL samples) (12) and other clinical methods (e.g., cytology and histology; Fig. 5*B*).

We next determined how the DMR-2 measurements compared with flow cytometry and Western blot analysis (Fig. 5*C*). The same samples were subjected to DMR measurements, flow cytometry

and Western blot analysis. The R_2 changes ($\Delta R_2^{HER2}/\Delta R_2^{\varnothing}$) from DMR (requiring ≈$10^3$ cells) showed good agreement ($R^2 > 98\%$) with both flow cytometry (requiring ≈10^5 cells) and Western blot analysis (requiring ≈10^7 cells), demonstrating the analytical capability of DMR-2 technology. Importantly, the DMR-sensor required fewer cells than either of the other 2 approaches and gave results in a fraction of the time (<15 min).

In the absence of a single ubiquitous cancer marker, one strategy to minimize false-negative results is to profile putative cancer cells for multiple markers ("signature"). DMR can be adapted for such a multitarget detection scheme, because it can perform measurements on few cells in small sample volumes and in parallel. As proof-of-concept, we chose to detect 3 targets: EpCAM (CD326), EGFR (ERBB1, CD126), and HER2/*neu* (ERBB2, CD340). The maximum R_2 changes from 3 markers were then used to calculate and display aggregate malignancy scores for a given FNA (Fig. 5*D*). For overall tumor detection, DMR assays yielded false-negative rates of 57–72% for single targets and 28% for 2 targets, whereas the false-negative rate was negligible for 3 targets. The DMR assay can be expanded beyond these 3 targets to profile complex cancer signatures.

Discussion

DMR is a promising biosensor technology with unique advantages in a clinical setting. The technology requires minimal sample preparation, can perform assays in turbid/obscure media, can be adapted to profile different targets (DNA, protein, metabolites, cells), and has the capability for high-throughput operation. Here, we built on our earlier proof-of-principle experiments and developed a new-generation (DMR-2) system that employs MNP with high r_2 relaxivity and a new NMR probe. Together, these improve-
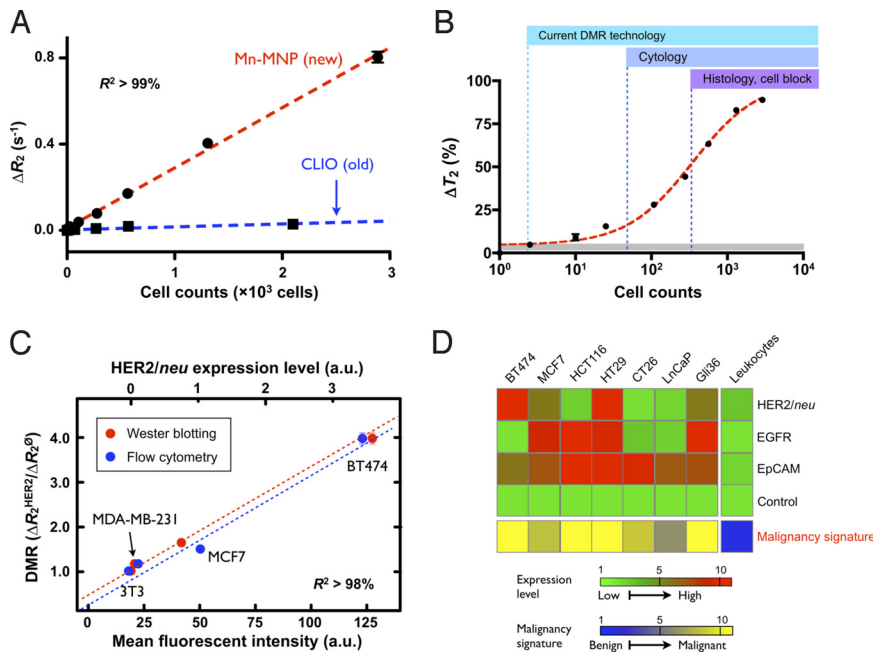
www.manaraa.com

Fig. 5. Tumor detection and profiling with DMR. (*A*) Different numbers of tumor cells (BT474) labeled with Mn-MNP-HER2 were introduced to a new DMR microfluidic chip for measurements. Excellent linear relationship ($R^2 > 99\%$) between the cell number and the transverse relaxation rate (R_2) was observed. When the MNP in the previous report (CLIO) were used, the sensitivity was lower by a factor of 10. (*B*) The DMR-2 showed detection limit nearly at the single-cell level (≈ 2 cells), superior to the current clinical methods (cytology and histology). (*C*) The analytical accuracy of the DMR assay was benchmarked against gold standards in molecular analysis, flow cytometry, and Western blot analysis, by measuring HER2/*neu* expression on breast cancer cells. The results reported by DMR showed good correlation ($R^2 > 98\%$) with the standard methods. Importantly, because of its high sensitivity, DMR required much fewer cells (10^3 cells per sample) compared with flow cytometry (10^5 cells) and Western blot analysis (10^7 cells). (*D*) A panel of xenograft tumors were subject to FNA, and profiled by DMR. The R_2 changes (ΔR_2) for 3 cancer makers (HER2/*neu*, EGFR, and EpCAM) were divided by the corresponding ΔR_2 with unmodified Mn-MNP to report the cellular expression levels. The maximum ratio among the 3 markers was used to determine the malignancy of a given aspirate. With multiple-marker targeting, the accuracy for correctly diagnosing cells as malignant could be considerably enhanced. All DMR measurements were in triplicate, and the data were displayed as mean ± SEM. ΔR_2 was calculated by taking R_2 differences between Mn-MNP targeted and corresponding control samples that had the same cell concentrations.

ments enhanced the detection sensitivity by >500-fold from the previous DMR-1 system (12). The specificity and analytical capability was further optimized by developing DMR assay protocols.

Using the improved DMR-2 system, we were able to determine the molecular expression of cancer cells in short time frames, an important advantage considering the growing recognition that cells removed from their native microenvironment rapidly change their phenotype (34). With its capability for fast and sensitive cell detection, the DMR-2 could become a useful tool for early detection and screening of cancer.

Although we focused our study on sensing major cell surface receptors, the DMR assay can be expanded to accommodate more targets or to interrogate complex cancer signatures. For example, it can be adapted to probe intracellular markers, signaling pathways, and the presence of key cytokines. With such capabilities, DMR can be further applied to monitor malignancy progression, metastases, or therapy resistance (35–37) in personalized patient care.

Methods

Synthesis of Mn-MNP. Iron (III) acetylacetonate [99.9%, Fe(acac)$_3$], manganese (II) acetylacetonate [Mn(acac)$_3$], oleylamine (70%), 1-octadecene (95%), 1,2-hexadecanediol (90%), chloroform (99%), sulfosuccinimidyl-(4-*N*-maleimidom-ethyl)cyclohexane-1-carboxylate (99%, sulfo-SMCC), 2,3-dimercaptosuccinic acid (98%, DMSA) and dimethyl sulfoxide (99.9%, DMSO) were purchased (Sigma–Aldrich) and used without further modification. Isopropanol (99.5%), hexane (98.5%), ethanol (99.5%), and NaHCO$_3$ were purchased (Fisher Scientific) and used as received.

First, we synthesized 10-nm Mn-MNP as a seed for the subsequent syntheses. Fe(acac)$_3$ (4 mmol, 1.4 g), Mn(acac)$_2$ (2 mmol, 0.5 g), 1,2-hexadecanediol (10 mmol, 2.9 g), oleic acid (6 mmol, 1.9 mL), oleylamine (6 mmol, 2.8 mL), and 1-octadecene (20 mL) were mixed by vigorous stirring under N$_2$ flow (1 h). The mixture was then heated and kept at 200 °C for 2 h. Subsequently, the temper-

ature was quickly elevated to 278 °C. The solution turned from dark brown to black at this point. After reflux, the mixture was cooled to room temperature, and isopropanol (80 mL) was added. Mn-MNP were collected via centrifugation (1,811 × g, 15 min) and then dispersed in hexane. Mn-MNP in a powder form was obtained by adding excess ethanol to Mn-MNP in hexane and collecting precipitates.

To make 12-nm Mn-MNP through the seed-mediated growth, 10-nm Mn-MNP (100 mg) were dissolved in hexane (10 mL) along with the same amount of metal acetylacetonates, 1,2-hexadecanediol, oleic acid, oleylamine, and 1-octadecene as described above. The mixture was heated and kept at 100 °C for 1 h under N$_2$ flow to remove hexane. The mixture was heated again and kept at 200 °C for 2 h. Finally, the temperature was increased to 300 °C, and the mixture was refluxed for 2 h before being cooled down to room temperature. The particles were then collected by the same washing and isolation procedure. In a similar manner, 16-nm Mn-MNP were synthesized by using 12-nm particles as a seed.

We characterized the morphology, structure, composition, and magnetic properties of Mn-MNP using a transmission electron microscope (TEM; JEOL 2100), an X-ray powder diffractometer (XRD; RU300; Rigaku), an inductively coupled plasma atomic emission spectrometer (ICP-AES; Activa-S; HORIBA Jobin Yvon) and a vibrating sample magnetometer (VSM; EV-5; ADE Magnetics), respectively.

Surface Modification of Mn-MNP and Antibody Conjugation. We first added ethanol to 16-nm Mn-MNP in hexane and centrifuged (1,811 × g, 10 min) the mixture. The precipitate (≈ 150 mg) was homogeneously redispersed in 10 mL of chloroform, and triethylamine (50 µL) was added. We then added DMSA (50 mg in 10 mL of DMSO) to the Mn-MNP solution. The mixture was shaken for 6 h at 37 °C and gradually turned heterogeneous. After centrifugation (1,811 × g, 10 min), the precipitate was washed with chloroform to remove excess DMSA, and dispersed in 10 mL of ethanol. DMSA (50 mg in 10 mL of DMSO) was added again to Mn-MNP in ethanol, and the whole process was repeated. The final precipitate (Mn-MNP-DMSA) was dispersed in 10 mL of H$_2$O. Ultimately, the particles were terminated with sulfhydryl (−SH) functional groups. The number of sulfhydryl group per Mn-MNP was ≈ 50 as determined by Ellman's reagent (Pierce Biotechnology).

Lee et al.

ENGINEERING

MEDICAL SCIENCES

www.manaraa.com

Monoclonal antibodies to cell surface markers (anti-HER2/neu: Herceptin; Genentech; anti-EGFR: Erbitux; Imclone Systems; anti-EpCAM: MAB9601; R&D Systems) were purchased and used without modification. To conjugate antibody, we first rendered them sulfhydryl active by attaching a maleimide functional group. We dissolved antibody (6 mg/mL) in 1 mL of PBS buffer, adjusted pH to 8.2 by adding 0.1 M $NaHCO_3$, and added 1 mg of sulfo-SMCC. The mixture was then incubated for 30 min at 37 °C. The sulfhydryl-active antibody was purified with PD-10 desalting column (GE Healthcare Bio-Sciences) and immediately combined with Mn-MNP-DMSA (5 mg/mL). The mixture was shaken for 6 h at 4 °C, followed by purification by using Sephadex G-100 (DNA grade; GE Healthcare Bio-Sciences). The number of antibodies per Mn-MNP was ≈10 as determined by bicinchoninic acid assay (BCA protein assay kit; Pierce Biotechnology).

Fabrication of NMR Probes. To embed solenoidal microcoils along with microfluidic channels, we adopted a molding technique for device fabrication. First, an insulated wire (diameter ≈160 μm) was wound around a polyethylene tubing (diameter ≈960 μm) to make a solenoidal coil. The coil-wound tubes were then placed on a custom-machined metal mold, and the mold was filled with polydimethylsiloxane (PDMS; Sylgard 184; Dow–Corning). After PDMS cure, the tubes were withdrawn to open up fluidic channels; the solenoidal coils were retained in PDMS supports. The device thus had a filling factor ≈1, which lead to high NMR signal levels.

DMR Measurements. The NMR probe was mounted on a printed circuit board along with RF amplifiers and fluidic fixture. To obtain a complete NMR system, the board was packaged into a miniaturized DMR setup as previously described (12). All DMR measurements were performed at the polarizing magnetic field of $B_0 = 0.5$ T generated by a portable permanent magnet. Transverse relaxation rate (R_2) was measured on 1-μL sample volumes, by using Carr–Purcell–Meiboom–Gill pulse sequences with the following parameters: echo time, 4 ms; repetition time, 6 s; the number of 180° pulses per scan, 500; the number of scans, 8. For ΔR_2 calculation, we took R_2 differences between a MNP-targeted and a cell number-matched control sample. All measurements were done in triplicate, and data were displayed as mean ± standard error.

Fluorescent Detection of Endogenous Cells. Leukocytes (10^7 cells per milliliter) prelabeled with CFSE (carboxyfluorescein diacetate succinimidyl ester) were mixed with cancer cells (SkBr3; 10^6 cells per milliliter). The mixture was incubated with fluorescent Mn-MNP-HER2 (5 min), washed to remove unbound MNP, and imaged (Eclipse 80I; Nikon). For flow cytometry, the mixtures were further incubated with a mixture of antibodies that allowed characterization of different cell populations (38). Data were collected on a LSRII (BD Biosciences) and analyzed with FlowJo v.8.5.2 (Tree Star, Inc.).

Xenograft Tumor Model. Tumor cells were cultured to ≈70% confluence, detached, and suspended in protease-free PBS solution. For breast cancer cell lines (BT474 and MCF7), ≈10^6 cells were mixed with 150 μL of Matrigel (#356230; BD Sciences) per tumor site. The mixture was then orthotopically implanted into the mammary fat pads of female C57BL/6 nude mice (The Jackson Laboratories) that had a 17β-estradiol pellet (0.72 mg; Innovative Research) s.c. implanted 7 days before tumor cell inoculation. For other cell lines, ≈10^6 cells per tumor were s.c. implanted on the back of female C57BL/6 nude mice; the prostate cancer cells (LnCaP) were implanted into a male mouse (COX7, MGH breeding colony). Mice were housed and maintained under aseptic conditions according to guidelines set by the Institutional Animal Care and Use Committee.

FNA Protocols. When the tumor reached ≈1 cm in size, they were aspirated by using 22-G needles. After the aspiration, the needle was washed in cell-dissociation solution (Cellstripper; Mediatech) to dislodge cells. Four needle washes per tumor were combined and then equally divided into five 1-mL aliquots. Four aliquots were incubated with unmodified or target-specific Mn-MNP (HER2/neu, EGFR, and EpCAM) under identical conditions (5 min at 37 °C with 50 μg·mL^{-1} [Fe+Mn]). Subsequently, excess Mn-MNP were removed by triple washes via centrifugation (200 × g, 5 min), and cell pellets were resuspended in PBS (1 mL). As a control, the fifth aliquot was prepared in a similar manner but without MNP incubation.

ICP-AES Measurements to Determine Particle Number per Cell. Needle aspirates of a breast tumor (BT474) were incubated with Mn-MNP conjugated with HER2/neu antibodies (37 °C, 5 min). Reference samples were prepared without MNP targeting. All samples were triple-washed with centrifugation (200 × g, 5 min) and dissolved in ICP-grade hydrochloric acid and 3% H_2O_2 (Fisher Scientific). Metal (Fe and Mn) concentrations were then analyzed by ICP-AES. From the result, the number of Mn-MNP was estimated, assuming that each particle had 2.2×10^4 metal atoms.

1. Kingsmore S (2006) Multiplexed protein measurement: Technologies and applications of protein and antibody arrays. *Nat Rev Drug Discov* 5:310–320.
2. Sawyers C (2004) Targeted cancer therapy. *Nature* 432:294–297.
3. Etzioni R, et al. (2003) The case for early detection. *Nat Rev Cancer* 3:243–252.
4. Nagrath S, et al. (2007) Isolation of rare circulating tumour cells in cancer patients by microchip technology. *Nature* 450:1235–1239.
5. Cheng MM, et al. (2006) Nanotechnologies for biomolecular detection and medical diagnostics. *Curr Opin Chem Biol* 10:11–19.
6. Tibbe A, et al. (1999) Optical tracking and detection of immunomagnetically selected and aligned cells. *Nat Biotechnol* 17:1210–1213.
7. Wang M, et al. (2005) Microfluidic sorting of mammalian cells by optical force switching. *Nat Biotechnol* 23:83–87.
8. Stern E, et al. (2007) Label-free immunodetection with CMOS-compatible semiconducting nanowires. *Nature* 445:519–522.
9. Zheng G, Patolsky F, Cui Y, Wang W, Lieber C (2005) Multiplexed electrical detection of cancer markers with nanowire sensor arrays. *Nat Biotechnol* 23:1294–1301.
10. Baselt D, et al. (1998) A biosensor based on magnetoresistance technology. *Biosens Bioelectron* 13:731–739.
11. Osterfeld S, et al. (2008) Multiplex protein assays based on real-time magnetic nanotag sensing. *Proc Natl Acad Sci USA* 105:20637–20640.
12. Lee H, Sun E, Ham D, Weissleder R (2008) Chip-NMR biosensor for detection and molecular analysis of cells. *Nat Med* 14:869–874.
13. Gueron M (1975) Nuclear-relaxation in macromolecules by paramagnetic-ions—Novel mechanism. *J Mag Reson* 19:58–66.
14. Buley I, Roskell D (2000) Fine-needle aspiration cytology in tumour diagnosis: Uses and limitations. *Clin Oncol* 12:166–171.
15. Roskell D, Buley I (2004) Fine needle aspiration cytology in cancer diagnosis. *Br Med J* 329:244–245.
16. Brooks R, Moiny F, Gillis P (2001) On T2-shortening by weakly magnetized particles: The chemical exchange model. *Magn Reson Med* 45:1014–1020.
17. Chithrani B, Chan W (2007) Elucidating the mechanism of cellular uptake and removal of protein-coated gold nanoparticles of different sizes and shapes. *Nano Lett* 7:1542–1550.
18. Jun Y, Lee J, Cheon J (2008) Chemical design of nanoparticle probes for high-performance magnetic resonance imaging. *Angew Chem Int Ed Engl* 47:5122–5135.
19. Laurent S, et al. (2008) Magnetic iron oxide nanoparticles: Synthesis, stabilization, vectorization, physicochemical characterizations, and biological applications. *Chem Rev* 108:2064–2110.
20. Shaw S, et al. (2008) Perturbational profiling of nanomaterial biologic activity. *Proc Natl Acad Sci USA* 105:7387–7392.
21. Jun YW, et al. (2005) Nanoscale size effect of magnetic nanocrystals and their utilization for cancer diagnosis via magnetic resonance imaging. *J Am Chem Soc* 127:5732–5733.
22. Lee J, et al. (2007) Artificially engineered magnetic nanoparticles for ultra-sensitive molecular imaging. *Nat Med* 13:95–99.
23. Park J, et al. (2004) Ultra-large-scale syntheses of monodisperse nanocrystals. *Nat Mater* 3:891–895.
24. Sun S, et al. (2004) Monodisperse MFe_2O_4 (M = Fe, Co, Mn) nanoparticles. *J Am Chem Soc* 126:273–279.
25. Tromsdorf UI, et al. (2007) Size and surface effects on the MRI relaxivity of manganese ferrite nanoparticle contrast agents. *Nano Lett* 9:2422–2427.
26. Morales M, et al. (1999) Surface and internal spin canting in Fe_2O_3 nanoparticles. *Chem Mater* 11:3058–3064.
27. Webb AG (1997) Radiofrequency microcoils in magnetic resonance. *Progr NMR spectr* 31:1–42.
28. Moore A, Weissleder R, Bogdanov AJ (1997) Uptake of dextran-coated monocrystalline iron oxides in tumor cells and macrophages. *J Magn Reson Imaging* 7:1140–1145.
29. Weissleder R, Cheng H, Bogdanova A, Bogdanov AJ (1997) Magnetically labeled cells can be detected by MR imaging. *J Magn Reson Imaging* 7:258–263.
30. Schwalbe M, Pachmann K, Hoffken K, Clement J (2006) Improvement of the separation of tumour cells from peripheral blood cells using magnetic nanoparticles. *J Phys Cond Matter* 18:S2865–S2876.
31. Besse P, Boero G, Demierre M, Pott V, Popovic R (2002) Detection of a single magnetic microbead using a miniaturized silicon Hall sensor. *Appl Phys Lett* 80:4199–4201.
32. Ejsing L, et al. (2004) Planar Hall effect sensor for magnetic micro- and nanobead detection. *Appl Phys Lett* 84:4729–4731.
33. Grossman H, et al. (2004) Detection of bacteria in suspension by using a superconducting quantum interference device. *Proc Natl Acad Sci USA* 101:129–134.
34. Durr E, et al. (2004) Direct proteomic mapping of the lung microvascular endothelial cell surface in vivo and in cell culture. *Nat Biotechnol* 22:985–992.
35. Imai K, Takaoka A (2006) Comparing antibody and small-molecule therapies for cancer. *Nat Rev Cancer* 6:714–727.
36. Iwenofu O, et al. (2008) Phospho-S6 ribosomal protein: A potential new predictive sarcoma marker for targeted mTOR therapy. *Mod Pathol* 21:231–237.
37. McCubrey J, et al. (2007) Roles of the Raf/MEK/ERK pathway in cell growth, malignant transformation and drug resistance. *Biochim Biophys Acta* 1773:1263–1284.
38. Swirski F, et al. (2007) Ly-6Chi monocytes dominate hypercholesterolemia-associated monocytosis and give rise to macrophages in atheroma. *J Clin Invest* 117:195–205.

www.manaraa.com